

Modeling of two-scale array microstructure and prediction of apparent contact angle based on WEDM

Zhaolong Li (✉ lizhaolong@hrbust.edu.cn)

Harbin University of Science and Technology

Yingtao Liu

Wangwang Li

Bingren Cao

Ye Dai

Research Article

Keywords: WEDM, Micro-nano structure, FEM, Modeling, Apparent contact angle prediction

Posted Date: May 17th, 2022

DOI: <https://doi.org/10.21203/rs.3.rs-1636625/v1>

License:  This work is licensed under a Creative Commons Attribution 4.0 International License.

[Read Full License](#)

Modeling of two-scale array microstructure and prediction of apparent contact angle based on WEDM

Zhaolong Li^{1,2}, Yingtao Liu², Wangwang Li², Bingren Cao², Ye Dai^{1,2}

1 Key Laboratory of Advanced Manufacturing Intelligent Technology of Ministry of Education, Harbin University of Science and Technology, Harbin, Heilongjiang Province 150080, China

2 School of Mechanical and Power Engineering, Harbin University of Science and Technology, Harbin, Heilongjiang Province 150080, China

Corresponding Author: lizhaolong@hrbust.edu.cn

Abstract

The core issue in the theoretical design of superhydrophobic surfaces is to elucidate the relationship between surface microstructure and wettability. In this paper, four two-scale array microstructure models with different shapes are proposed to predict the apparent contact angles (CAs) of EN-GJL-250 (Grey Cast Iron) surface under different Wire-cut electrical discharge machining (WEDM) discharge parameters. The primary microstructure is the artificially designed semicircle, rectangular, sawtooth and square column array microstructure, and the secondary microstructure is the micro-nano structure of the surface machined by WEDM. Firstly, the mechanical analysis of water droplets placed on the primary array microstructure is carried out by the force balance method. According to Newton's third law, equations containing CA parameters are listed. Secondly, the finite element method (FEM) was used to analogue simulation the distribution of material surface temperature and flow field in the WEDM single pulse discharge machining process. The surface equivalent geometric model of WEDM was established by a uniform arrangement of single pulse pits obtained by simulation, the surface roughness coefficients under different discharge parameters were calculated, and the influence of the surface roughness coefficients on the surface wettability was studied. The numerical results show that the CA is jointly determined by the surface roughness coefficient under different discharge parameters, and the shape and size parameters of the microstructure. Finally, semicircle, rectangular, sawtooth and square column array microstructures were fabricated on EN-GJL-250 surface by high-speed WEDM. Experimental results show: The CA of water droplets on the square column array microstructure is the largest, the predicted values of the CA were in good agreement with the experimental values, and the average relative error was 7.83 %.

Keywords: WEDM; Micro-nano structure; FEM; Modeling; Apparent contact angle prediction.

1. Introduction

Metallic materials are widely used in construction, ships, bridges, power and other industries. However, in the use process, metal materials due to corrosion, icing and other

problems affect the performance of equipment [1-2], and even safety risks. The reasons for the above hidden dangers are attributed to an important feature of solid surface -- wettability [3-5], which is jointly determined by the chemical composition and microscopic geometric structure

of material surface [6-7]. For a long time, researchers have shown great interest in how to control the micro-nano structure of solid materials to control their wetting properties (such as superhydrophobicity). Superhydrophobic surface refers to a kind of special surface with CA greater than 150° and rolling angle less than 10° . The construction of the superhydrophobic surface on the metal substrate can effectively alleviate the problems such as non-corrosion resistance and easy icing in the use process, and can also endow it with special functions such as self-cleaning, oil-water separation, lubrication and drag reduction [8–12]. However, it is a fundamental problem to obtain and maintain superhydrophobic properties on metal surfaces: how to subjectively regulate the superhydrophobic properties of material interfaces? Since most metal materials have high surface energy [13] and show obvious hydrophilicity, it is more difficult to prepare superhydrophobic surfaces with metal as the substrate than with glass and low surface energy polymers.

The preparation of superhydrophobic surface includes the construction of rough microstructure and the reduction of surface free energy. At present, the methods for preparing micro-nano structures on the metal surfaces include the template method, nano-spraying method, electrochemical machining method, etching method [17–18], sol-gel method, etc. However, these methods are complex operations or expensive equipment, which limits the industrial production of metal-based superhydrophobic surfaces. WEDM is a special machining method widely used in industry. It has the advantages of mature equipment, high process reliability, high automation, low processing cost and environmental protection. Importantly,

WEDM is easier to fabricate metal surfaces with both micron and nano-composite structures, and the size of the microstructure can be controlled by adjusting the processing parameters, which provides the possibility of manufacturing multi-scale microstructures [20-26]. For example, Xiao et al. [27] processed the array microcolumn structure on the surface of aluminum alloy by WEDM, and then deposited nanoparticles on the microcolumn combined with an electrochemical method to directly obtain the superhydrophobic surface. Xiong et al. [28] constructed a micro-nano structure by HS-WEDM, and then immersed the workpiece in stearic acid ethanol solution to prepare the superhydrophobic copper substrate surface. Wu et al. [29] prepared sinusoidal and rectangular microstructures on copper alloy surfaces by WEDM. It was found that due to the special material removal method of WEDM, the surface of the workpiece after machining has a multi-scale microstructure, which improves the hydrophobicity of the copper alloy surface. The maximum contact angles of sinusoidal and rectangular structures can reach 152.1° and 149.1° , respectively. Dong et al. [30] prepared the micro-nano hierarchical structure on the surface of beryllium copper alloy by micro-EDM and carbon deposition. Oil treatment was then performed to enhance the surface strength. The prepared surface exhibits excellent superhydrophobic properties.

The preparation method of the superhydrophobic surface has been relatively mature, but the theoretical research is still lagging behind. The superhydrophobic properties of the prepared surface can only be measured by instruments. To obtain the ideal superhydrophobic surface, a series of size parameters experiments are often needed, which

increases the cost of preparing the superhydrophobic surface. A theoretical model was established to predict the CA of the metal materials. By changing the shape and size of the surface microstructure, the surface wettability can be adjusted according to the actual needs, to guide the preparation of superhydrophobic surfaces [33-34]. Taking spherical microstructure as an example, Extrand et al. [31] studied the influence of spherical structure parameters on surface wettability by force balance theory. The results show that decreasing the sphere radius is beneficial to increasing the droplet contact Angle, and increasing the sphere radius breaks the static equilibrium between the droplet gravity and capillary action, and destroys hydrophobicity. Liu et al. [32] analyzed the influence of geometric parameters of array square columns on the transition between compound and non-compound wetting states of droplets from the perspective of energy. The results show that increasing the width and height of micropillars and decreasing the spacing of micropillars is beneficial to the formation of a stable Cassie wetting state. However, the existing theoretical design of micro-nano structures on superhydrophobic surfaces is mainly aimed at the ordered microstructure at a single scale, and there are few composites (two-stage) micro-nano structures on superhydrophobic surfaces. Establishing the CA prediction model for multi-scale microstructures helps to determine more practical and effective design criteria for hydrophobic structures [35]. Wang et al. [36] proposed a numerical calculation method for the water contact angle on the microstructure of the groove array by using the layered model. Firstly, the mechanical analysis of water droplets placed in the array microstructure was carried out, and then the wettability of

WEDM surface morphology was evaluated. The established mathematical model can predict the contact angle under different geometric sizes. Dong et al. [37] proposed a numerical method combined with a nonlinear optimization algorithm to numerically calculate the contact angle, contact angle hysteresis and state transfer barrier of droplets.

To prepare the controllable superhydrophobic surface by WEDM, the CA prediction model of two-scale array microstructure was established, and the influence of microstructure shape and microstructure size parameters on the CA was analyzed. At the same time, the single pulse discharge crater morphology under different discharge parameters of WEDM was simulated by FEM, and the geometric equivalent model of EN-GJL-250 WEDM surface was constructed to evaluate the wettability of WEDM surface morphology under different discharge parameters. Finally, the micro-structure cutting experiment was carried out on the EN-GJL-250 workpiece using WEDM technology to prepare the superhydrophobic surface. In this study, microstructure shape, peak current and pulse width were taken as input parameters, and CA was taken as output parameter. The accuracy of the WEDM dual-scale array microstructure model in predicting CA was verified by experiments. According to the theoretical model, the controllable preparation of superhydrophobic surface by WEDM can be realized.

2. Apparent contact angle prediction model of primary array microstructure

In the process of studying the wettability of the metal surfaces, it is found that the CA of water droplets on the metal surfaces is related to the microstructure shape and size parameters. To

explain the above problems, based on the Cassie-Baxter model, this section analyzes the force balance of water droplets on four different shape microstructures: rectangle, square column, sawtooth and semicircle. Here, the micro-nano structure of the WEDM machined surface is ignored when constructing the primary array microstructure. The geometry and size of four primary array microstructures are shown in Fig. 1.

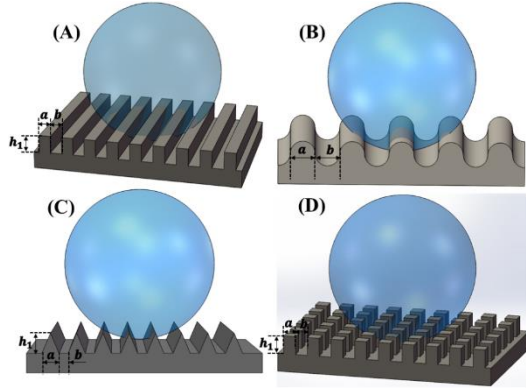


Fig. 1 Geometric dimensions of array microstructures. (A) Rectangular; (B) Semicircular; (C) Sawtooth; (D) Square column.

When water droplets drop on the microstructure, the original spherical droplets will deform under the combined action of gravity, support force and surface tension. Experiments show that the EN-GJL-250 material has hydrophobic properties after WEDM and low surface energy treatment. In other words, water droplets can maintain a stable spherical shape on the material surface. In view of this situation, a mathematical theoretical model is established to predict the CA. To simplify the calculation, the model is simplified as follows:

1. The array microstructures are uniformly distributed in the X-direction, and the size and shape of each microstructure are identical;

2. The droplet is spherically missing and the radius of the droplet does not change before and after the droplet falls on the surface of the workpiece.

3. Neglecting the effect of gravity load along the radial direction of the droplet.

4. The total volume of droplets remains constant and the reduced volume of droplets exists in the gap between microstructures.

5. The wetting state of the droplet on the microstructure is the Cassie-Baxter state.

6. The contact area between droplets and air in the microstructure gap is semicircular.

7. A droplet drops onto a microstructure that is symmetric with one of the microstructures.

8. The internal cohesion of the droplet is constant.

2.1 Apparent contact Angle prediction model for rectangular array microstructures

The dimensional parameters and force analysis of the spherical droplet on the microstructure is shown in Fig. 2, and the relationship between the parameters is given by Eq (1-4):

$$\theta_s = \theta + \pi/2 \quad (1)$$

$$R_1 = R \cos \theta = R \sin \theta_s \quad (2)$$

$$h = R \sin \theta = -R \cos \theta_s \quad (3)$$

$$H = R + h = R(1 - \cos \theta_s) \quad (4)$$

Where R is the radius of ball-shaped droplets; R_1 is the three-phase contact line radius of the droplet on micro-structure; θ is the angle between R and R_1 ; θ_s is the CA of droplets; h is the distance between droplet center and microstructure plane; H is the distance between droplet tip and microstructure plane.

The model uses the force balance method to establish the equation that, the CA is determined based on the geometric parameters of the array microstructure. Water droplets are always in equilibrium on the array microstructure, and the forces applied on the droplets are analyzed mainly in the X and Z directions. The droplet is in a

balanced state of four forces on the rectangular microarray structure, in which the four forces are: the support force of the microstructure pillar on the droplet F_{sl} , the surface tension of the droplet at the microstructure gap F_{gl} , the surface tension

at the edge of the three-phase contact line F and the gravity of the droplet G . The relationship between the forces is given by Eq. 5.

$$G = F_{sl} + F_{gl} + F \sin(\pi - \theta_s) \quad (5)$$

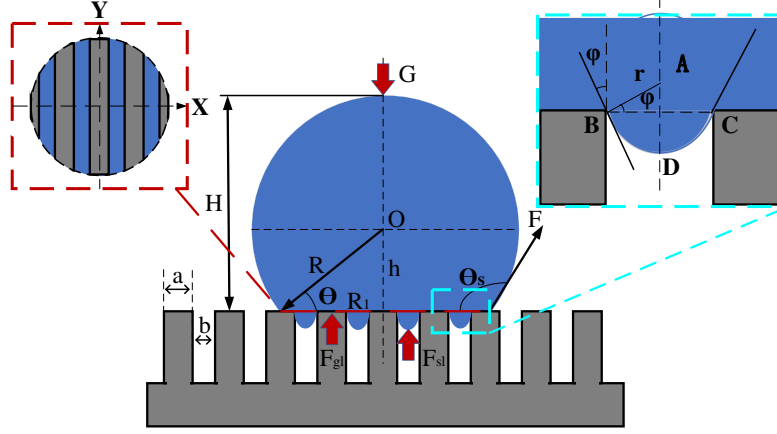


Fig. 2 Diagram of force analysis of water droplet on rectangular array microstructure.

In the rectangular array microstructure, T represents the length of a single period, $2n$ represents the total number of periods of the array microstructure, and the brackets represent the downward integration. The T and n are calculated according to Eq.6 and Eq.7.

$$T = a + b \quad (6)$$

$$n = \left\lceil \left(R_1 + \frac{b}{2} \right) / T \right\rceil \quad (7)$$

Where a is the width of a single rectangular microcolumn; b is the gap width between rectangular microcolumns.

2.1.1 Calculation of the support force of the microstructure pillar on the droplet F_{sl}

According to Newton's third law, the value of F_{sl} is equal to the gravity of the liquid column on the rectangular microstructure. To calculate the gravity of the liquid column on a single microstructure, it is necessary to obtain the contact area S_s between the droplet and the solid part, as shown in Fig. 2. Calculate S_s according to Eq.8.

$$S_s = S_c - S_l \quad (8)$$

Where S_l is the total area of the gas-liquid contact part; S_c is the total area of droplet contact with the metal surface.

The contact plane between the droplet and the microstructure can be regarded as a circle and can be expressed by Eq.9. Using the idea of calculus to calculate S_l is more in line with the actual situation. The calculation formula is as follows:

$$x^2 + y^2 = R_1^2 \quad (9)$$

$$S_{l-1} = 2 \int_0^{\frac{b}{2}} \sqrt{(R_1^2 - x^2)} dx \quad (10)$$

$$S_{l-2} = 2 \int_{T-\frac{b}{2}}^{T+\frac{b}{2}} \sqrt{(R_1^2 - x^2)} dx \quad (11)$$

.....

$$S_{l-n} = 2 \int_{(n-1)T-\frac{b}{2}}^{(n-1)T+\frac{b}{2}} \sqrt{(R_1^2 - x^2)} dx \quad (12)$$

The S_l can be calculated according to Eq. 13.

$$S_l = \sum_{i=0}^n S_{l-i} = 2 \int_0^{\frac{b}{2}} \sqrt{(R_1^2 - x^2)} dx + 2 \sum_{i=1}^{n-1} \int_{iT-\frac{b}{2}}^{iT+\frac{b}{2}} \sqrt{(R_1^2 - x^2)} dx \quad (13)$$

The S_c can be calculated according to Eq. 14.

$$S_c = \pi R_1^2 \quad (14)$$

The average height of the liquid column on rectangular microstructure \bar{H} can be calculated according to Eq. 15.

$$\frac{4}{3}\pi R^3 = \pi R_1^2 \bar{H} \quad (15)$$

Therefore, the F_{sl} can be calculated according to Eq. 16.

$$F_{sl} = \rho g (S_c - S_l) \bar{H} = \rho g (\pi R_1^2 - \sum_{i=0}^n S_{l-i}) \frac{4R^3}{3R_1^2} \quad (16)$$

Where ρ is the density of water; g is the acceleration of gravity.

2.1.2 Calculation of the surface tension of microstructure gaps on droplets F_{gl}

Because the wetting state of the droplets on the microstructure surface is the Cassie-Baxter state, the shape of the droplets in the gap is similar to an arc. As shown in Fig. 2. φ is the angle between the arc tangent of the droplet in the microstructure gap and the Z direction. To determine F_{gl} , the angle φ must be calculated first. Assume that the O (0,0) is the origin of the coordinate system, A (k, p) is the center of the arc, B (0,0), C ($b,0$) and D ($\frac{b}{2}, -v$) are three points on the arc, and r is the radius of the arc.

$$k^2 + p^2 = r^2 \quad (17)$$

$$\left(\frac{b}{2} - k\right)^2 + (-v - p)^2 = r^2 \quad (18)$$

$$(b - k)^2 + p^2 = r^2 \quad (19)$$

Combine the above three formulas, the r is calculated according to Eq. 20.

$$r = \sqrt{\left\{ \frac{b^2}{4} + \frac{1}{4v^2} \left[\frac{b^2}{4} - v^2 \right]^2 \right\}} \quad (20)$$

Where v is distance between minimum point of droplet penetration gap and metal plane. The φ is calculated according to Eq. 21.

$$\varphi = \cos^{-1} \frac{b}{2 \sqrt{\left\{ \frac{b^2}{4} + \frac{1}{4v^2} \left[\frac{b^2}{4} - v^2 \right]^2 \right\}}} \quad (21)$$

The action direction of the droplet surface tension

is along the tangent direction of the droplet and the solid contact point at the gap. The two sides of the force projected in the X direction are balanced. As long as the force in the Z direction is obtained, the force F_{gl} can be obtained. The crude line in the red range in Fig. 2 is the gas-liquid contact line. The gap force F_{gl-1} of the first cycle is calculated according to Eq. 22.

$$F_{gl-1} = 4\sigma_{gl} \cos \varphi \left(\sqrt{\left[R_1^2 - \frac{b^2}{4} \right]} + \sqrt{\left[R_1^2 - \left(T - \frac{b}{2} \right)^2 \right]} \right) \quad (22)$$

Where σ_{gl} is the gas-liquid surface tension coefficient. In the subsequent calculations, the distance of the array microstructure from the droplet center in the X-direction increases sequentially by one cycle T in length. The calculation equation is shown as follows. (Eq. 23 and 24).

$$F_{gl-2} = 4\sigma_{gl} \cos \varphi \left(\sqrt{\left[R_1^2 - \left(T + \frac{b}{2} \right)^2 \right]} + \sqrt{\left[R_1^2 - \left(2T - \frac{b}{2} \right)^2 \right]} \right) \quad (23)$$

.....

$$F_{gl-n} = 2\sigma_{gl} \cos \varphi \left(\sqrt{\left[R_1^2 - \left((n-1)T + \frac{b}{2} \right)^2 \right]} + \sqrt{\left[R_1^2 - \left(nT - \frac{b}{2} \right)^2 \right]} \right) \quad (24)$$

Therefore, the F_{gl} can be calculated according to Eq. 25.

$$F_{gl} = \sum_{i=0}^n F_{gl-i} - F_{gl-n} = 4\sigma_{gl} \cos \varphi \sum_{i=1}^n \sqrt{\left[R_1^2 - \left(\frac{(2i-1)T}{2} \right)^2 \right]} \quad (25)$$

2.1.3 Calculation of the surface tension of three-phase contact line edge F

The semicircle length of the three-phase contact part L (excluding the contact line and

both sides of the microstructure that overlap with the coordinate origin) is equal to the product of the radius of the three-phase contact circle and the corresponding central angle. The calculation equation is shown as follows. (Eq. 26 and 28).

$$L_0 = 2R_1 \sin^{-1} \frac{R_1 - \frac{b}{2}}{R_1} \quad (26)$$

$$L_1 = 4R_1 \left(\sin^{-1} \frac{T - \frac{b}{2}}{R_1} - \sin^{-1} \frac{\frac{b}{2}}{R_1} \right)$$

.....

$$L_n = 4R_1 \left(\sin^{-1} \frac{nT - \frac{b}{2}}{R_1} - \sin^{-1} \frac{(n-1)T + \frac{b}{2}}{R_1} \right) \quad (27)$$

Therefore, the F can be calculated according to Eq. 28.

$$F = 4R_1 \sigma_{gl} \left[2R_1 \sin^{-1} \frac{R_1 - \frac{b}{2}}{R_1} + \sum_{i=0}^n \left(\sin^{-1} \frac{(i+1)T - \frac{b}{2}}{R_1} - \sin^{-1} \frac{iT + \frac{b}{2}}{R_1} \right) \right] \quad (28)$$

Therefore, without considering the rough surface morphology of WEDM, Eq. 5, 16, 25 and 28 are combined to obtain Eq. 29, the θ_s can be calculated according to Eq. 28.

$$\begin{aligned} \frac{4}{3} \pi R^3 \rho g &= \rho g \left(\pi R_1^2 - 2 \int_0^{\frac{b}{2}} \sqrt{(R_1^2 - x^2)} dx - \right. \\ &2 \sum_{i=1}^{n-1} \int_{iT - \frac{b}{2}}^{iT + \frac{b}{2}} \sqrt{(R_1^2 - x^2)} dx \left. \right) \frac{4R^3}{3R_1^2} + \\ &4\sigma_{gl} \cos \varphi \sum_{i=1}^n \sqrt{\left[R_1^2 - \left(\frac{(2i-1)T}{2} \right)^2 \right]} + \\ &4R_1 \sigma_{gl} \cos \theta \left[2R_1 \sin^{-1} \frac{R_1 - \frac{b}{2}}{R_1} + \right. \\ &\left. \sum_{i=0}^n \left(\sin^{-1} \frac{(i+1)T - \frac{b}{2}}{R_1} - \sin^{-1} \frac{iT + \frac{b}{2}}{R_1} \right) \right] \quad (29) \end{aligned}$$

2.2 Apparent contact angle prediction model for semicircle array microstructures

To theoretically explore the influence of the shape of microstructure on the CA under the same parameters, the following assumptions were made in this study:

1. Contact radius of a droplet on semicircular array microstructure (R_1) is the same as that on

rectangular microstructure;

2. The protruding semicircular microstructure is in a state of complete wetting.

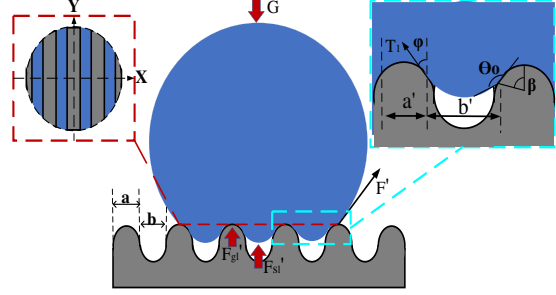


Fig. 3 Diagram of force analysis of water droplet on semicircular array microstructure.

The shape of microstructure is a single variable, and the basic size of semicircle microstructure is consistent with that of rectangular microstructure. The radius of the semi-circular microstructure is $\frac{a}{2}$, the radius of the semi-circular gap is $\frac{b}{2}$, and the depth of the microstructure is $\frac{a+b}{2}$ (far greater than the height v of the small droplet penetrating the gap). The direction of each force of a droplet on a semicircular array microstructure is shown in Fig.3. The relationship between the forces is given by Eq. 30.

$$G = F_{sl}' + F_{gl}' + F' \sin(\pi - \theta_s) \quad (30)$$

Compared with the rectangular microstructure, the actual support area of droplets on the semicircular array microstructure pillar has changed, as shown in Fig. 3. The liquid pressure points to the inside of the microcolumn, and only the vertical component of the pressure is concerned here. The relationship between the parameters is given by Eq (31-33):

$$a_2 = a \sin \beta \quad (31)$$

$$b_2 = b + a(1 - \sin \beta) \quad (32)$$

$$n_2 = \left\lceil \left(R_1 + \frac{b_2}{2} \right) / T \right\rceil \quad (33)$$

Where a_2 is the actual contact width of droplets

on semicircular micropillars; b_2 is the gap width of a droplet on semicircular microstructure; β is the angle between the end point of the arc at the microstructure gap connecting the center of the circle and the Z-direction.

At the same time, compared with the microstructure of the rectangular array, the changing parameters include angle φ . The φ is calculated according to Eq. 34.

$$\varphi = \frac{3\pi}{2} - \theta_0 - \beta \quad (34)$$

Where θ_0 is the intrinsic contact angle of the material surface. Since none of the other parameters have changed, the CA of semicircular array microstructure is calculated according to Eq. 35.

$$\begin{aligned} \frac{4}{3}\pi R^3 \rho g &= \rho g \left(\pi R_1^2 - 2 \int_0^{\frac{b_2}{2}} \sqrt{(R_1^2 - x^2)} dx + \right. \\ & \left. 2 \sum_{i=0}^{n_2-1} \int_{iT-\frac{b_2}{2}}^{iT+\frac{b_2}{2}} \sqrt{(R_1^2 - x^2)} dx \right) \frac{4R^3}{3R_1^2} + \\ & 4\sigma_{gl} \cos \varphi \sum_{i=1}^{n_2} \sqrt{\left[R_1^2 - \left(\frac{(2i-1)T}{2} \right)^2 \right]} + \\ & 4R_1 \sigma_{gl} \cos \theta \left[2R_1 \sin^{-1} \frac{R_1 - \frac{b_2}{2}}{R_1} + \right. \\ & \left. \sum_{i=0}^{n_2} \left(\sin^{-1} \frac{(i+1)T - \frac{b_2}{2}}{R_1} - \sin^{-1} \frac{iT + \frac{b_2}{2}}{R_1} \right) \right] \quad (35) \end{aligned}$$

2.3 Apparent contact angle prediction model for sawtooth array microstructures

For special geometric microstructures such as sawtooth array microstructure, in the Cassie-Baxter state, the fraction of the contact area between the droplet and solid in the actual total contact area tends to zero, and the CA will reach the maximum at this time, which means that this array microstructure has ideal superhydrophobic performance. However, the contact shape between the droplet and the sawtooth array microstructure cannot completely change into linear contact. Therefore, under the premise of considering the special machining mode of

WEDM, this study considers that the contact shape between the droplet and the sawtooth array microstructure is a semicircle, and the semicircle radius is much smaller than the bottom of the sawtooth array microstructure, as shown in Fig. 4.

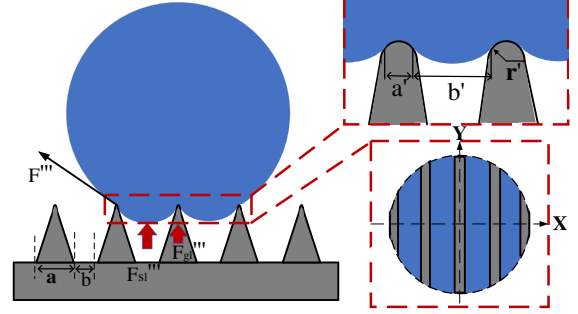


Fig. 4 Diagram of force analysis of water droplet on sawtooth array microstructure.

The relationship between the parameters is given by Eq (36-33):

$$r' = \delta a \quad (36)$$

$$a_3 = r' \sin \beta \quad (37)$$

$$b_3 = b + 2r'(1 - \sin \beta) \quad (38)$$

$$T_3 = a_3 + b_3 \quad (39)$$

$$n_3 = \left\lceil \left(R_1 + \frac{b_3}{2} \right) / T_3 \right\rceil \quad (40)$$

Where r' is the radius of half circle at the top of sawtooth shape; The value of δ is related to the actual machining accuracy of the surface microstructure, and the value of δ is always less than 1; a_3 is the actual contact width of the droplets on sawtooth micropillars; b_3 is the gap width of the droplet on sawtooth microstructure. The direction of each force of the droplet on a sawtooth array microstructure is shown in Fig.4. The relationship between the forces is given by Eq.41.

$$G = F_{sl}''' + F_{gl}''' + F''' \sin(\pi - \theta_s) \quad (41)$$

The relationship between force and parameters on sawtooth array microstructure is the same as that on semicircular microstructure.

The CA of the sawtooth array microstructure is calculated according to Eq. 42.

$$\begin{aligned} \frac{4}{3}\pi R^3 \rho g &= \rho g \left(\pi R_1^2 - 2 \int_0^{\frac{b_3}{2}} \sqrt{(R_1^2 - x^2)} dx + \right. \\ &2 \sum_{i=0}^{n_3-1} \int_{iT_3 - \frac{b_3}{2}}^{iT_3 + \frac{b_3}{2}} \sqrt{(R_1^2 - x^2)} dx \left. \right) \frac{4R^3}{3R_1^2} + \\ &4\sigma_{gl} \cos \varphi \sum_{i=1}^{n_3} \sqrt{\left[R_1^2 - \left(\frac{(2i-1)T_3}{2} \right)^2 \right]} + \\ &4R_1 \sigma_{gl} \cos \theta \left[\sum_{i=0}^{n_3} \left(\sin^{-1} \frac{(i+1)T_3 - \frac{b_3}{2}}{R_1} - \right. \right. \\ &\left. \left. \sin^{-1} \frac{iT_3 + \frac{b_3}{2}}{R_1} \right) + 2R_1 \sin^{-1} \frac{R_1 - \frac{b_3}{2}}{R_1} \right] \end{aligned} \quad (42)$$

2.4 Apparent contact angle prediction model for square column array microstructures

The direction of each force of a droplet on a square column array microstructure is shown in Fig. 5.

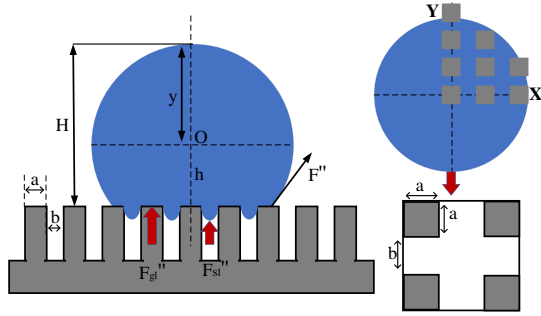


Fig. 5 Diagram of force analysis of water droplet on square column array microstructure.

The relationship between the forces is given by Eq. 43.

$$G = F_{sl}'' + F_{gl}'' + F'' \cos \theta \quad (43)$$

The supporting force of square column array microstructure pillar on droplet F_{sl}'' can be calculated according to Eq. 44.

$$F_{sl}'' = (h + \bar{y}) \times a^2 \times \frac{\pi R_1^2}{(a+b)^2} \times \rho g \quad (44)$$

Where $(h + \bar{y})$ is the average height of the water column on a single square column; a^2 is the solid-liquid contact area of a single square column; $\frac{\pi R_1^2}{(a+b)^2}$ is the number of the square columns in the contact area of droplet and square column array microstructure.

The shape of the droplet on the microstructure surface is a circular defect, and its expression is $x^2 + y^2 = R^2$. Based on Fig. 5, it is known that at the centre of the droplet (i.e., when $x = 0, y = R$), as x increases, the value of y changes appropriately. The calculation process of \bar{y} is as follows:

$$\begin{aligned} x_1 &= a + b & y_1 &= \sqrt{(R^2 - (a+b)^2)} \\ & & & \dots \dots \dots \\ x_n &= n(a+b) & y_n &= \sqrt{(R^2 - n^2(a+b)^2)} \\ \sum_{i=0}^n y_n &= \sum_{i=0}^n \sqrt{(R^2 - i^2(a+b)^2)} \\ \bar{y} &= \frac{\sum_{i=0}^n y_n}{n} = \frac{\sum_{i=0}^n \sqrt{(R^2 - i^2(a+b)^2)}}{n} \end{aligned} \quad (45)$$

Therefore, the F_{sl}'' can be calculated according to Eq. 46.

$$F_{sl}'' = \left(h + \frac{\sum_{i=0}^n \sqrt{(R^2 - i^2(a+b)^2)}}{n} \right) \times a^2 \times \frac{\pi R_1^2}{(a+b)^2} \times \rho g \quad (46)$$

The F_{gl}'' can be calculated according to Eq. 47.

$$F_{gl}'' = \frac{\pi R_1^2}{(a+b)^2} \times 4a \times \sigma_{gl} \times \cos \varphi \quad (47)$$

The F'' can be calculated according to Eq. 48.

$$\begin{aligned} F'' = F &= 4R_1 \sigma_{gl} \left[\sum_{i=0}^n \left(\sin^{-1} \frac{(i+1)T - \frac{b}{2}}{R_1} - \right. \right. \\ &\left. \left. \sin^{-1} \frac{iT + \frac{b}{2}}{R_1} \right) + 2R_1 \sin^{-1} \frac{R_1 - \frac{b}{2}}{R_1} \right] \end{aligned} \quad (48)$$

The CA of square column array microstructure is calculated according to Eq. 49.

$$\begin{aligned} \frac{4}{3}\pi R^3 \rho g &= \left(h + \frac{\sum_{i=0}^n \sqrt{(R^2 - i^2(a+b)^2)}}{n} \right) \times a^2 \times \\ &\frac{\pi R_1^2}{(a+b)^2} \times \rho g + \frac{\pi R_1^2}{(a+b)^2} \times 4a \times (\sigma_{gl} + \sigma_{sl}) \times \\ &\cos \Psi + 4R_1 \sigma_{gl} \left[\sum_{i=0}^n \left(\sin^{-1} \frac{(i+1)T - \frac{b}{2}}{R_1} - \right. \right. \\ &\left. \left. \sin^{-1} \frac{iT + \frac{b}{2}}{R_1} \right) + 2R_1 \sin^{-1} \frac{R_1 - \frac{b}{2}}{R_1} \right] \end{aligned} \quad (49)$$

3. Establishment of apparent contact angle prediction model for two-scale array microstructure

The research on the wettability of metal surface microstructure can be divided into two

parts. The first is a small microstructure, size between tens of microns to hundreds of microns. When the size of the microstructure is appropriate, the wetting state of water droplets on the surface of the material conforms to the Cassie-Baxter model. The microstructure divides the contact position of water droplets and the material into gas-liquid and solid-liquid parts. The other part is the rough micro-nano structure formed on the surface of the material after processing. The existence of a micro-nano structure will increase the contact area between water droplets and the material surface. According to the Wenzel model, the presence of roughness can enhance the bulk wettability of materials.

3.1 Calculation of surface roughness coefficient

3.1.1 WEDM single pulse discharge surface topography simulation

First, COMSOL Multiphysics 5.3 (COMSOL Inc., Burlington, MA, MSA), a commercial finite element software package, was used to simulate the thermal and flow field changes on the surface of the EN-GJL-250 material during the single-pulse discharge of WEDM. In this simulation model, the level set method is used to track the formation and growth process of single pulse discharge pits, and the size characteristics of discharge pits at different discharge times are studied. Selection of simulation parameters: discharge voltage is 24 V, discharge current is 12 A, pulse width is 32 μ s and duty cycle is 0.25. The total calculation time is 200 μ s, the discharge duration is 100 μ s, and the surface morphology of EN-GJL-250 material changes with time, as shown in Fig. 6. The simulation results show that in the process of forming the discharge pit, the molten material

will first form a smooth depression at the center, then be pushed to both sides and continuously etched away, and at the same time, flanging protrusions will appear at the periphery of the pit. At 100 μ s, the spark discharge time ended, but the size of the pits still tended to increase. Until 160 μ s, the depth and depth of the pits began to remain stable, and the flanging protrusions were basically smooth, and there was no sharp phenomenon.

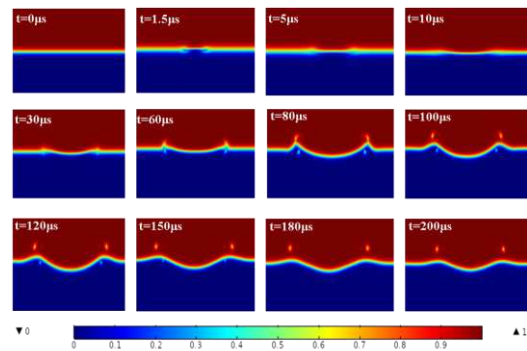


Fig.6 Formation process of single pulse discharge crater.

The final appearance of the discharge pits is shown in Fig. 7(A). To more intuitively analyze the variation law of crater morphology and feature size during the formation of single-pulse discharge craters, numerical simulations were carried out on the crater size under different discharge parameters, and a single-pulse discharge crater model was established, as shown in Fig. 7 (B).

3.1.2 Establishment of the geometric equivalent model of EN-GJL-250 WEDM surface

The surface morphology of WEDM is determined by numerous single pulse discharge pits and discharge positions. In the actual discharge process, the discharge position has randomness and disorder, as shown in Fig. 8.

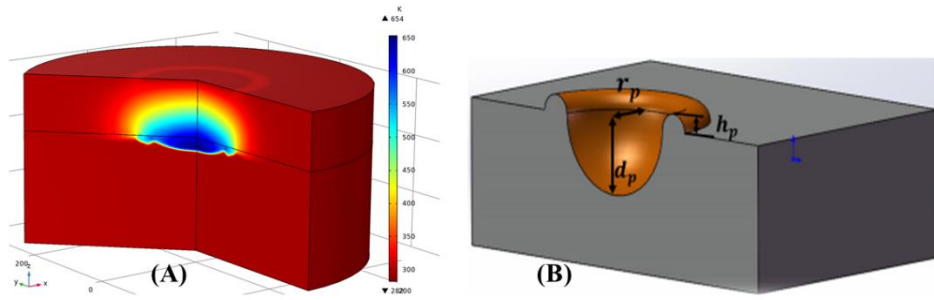


Fig. 7 (A) The temperature distribution around the hot etched pit at the end of single pulse discharge; (B) Single pulse discharge crater model.

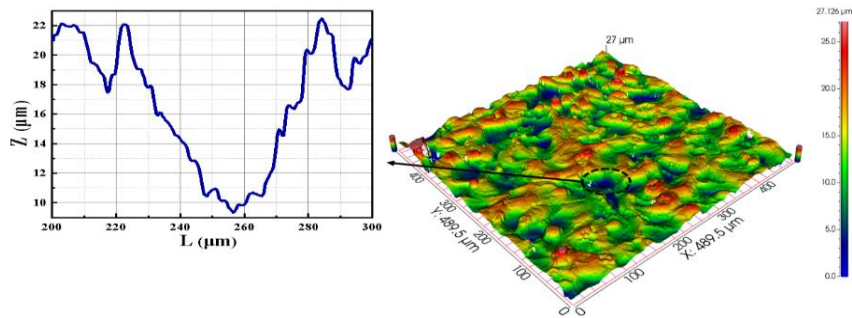


Fig. 8 Surface topography of WEDM continuous discharge: 3D view and crater shape and dimensions ($I_p=12A$, $T_{on}=32\mu s$).

Calculating the roughness coefficient of the surface of EN-GJL-250 after WEDM is very important for establishing the CA prediction model based on the Wenzel theory. To facilitate the calculation, the following assumptions are made about the shape and arrangement of pits:

- (1) The size of all pits is the final size of the pits on the back surface after WEDM single-pulse discharge simulation, and the pits are evenly arranged on the processing plane;
- (2) The shape of a complete pit is a part of a ball;
- (3) It is considered that the plane of the workpiece before machining is smooth;
- (4) Water droplets can completely cover the processed surface.

After making the above assumptions, the surface morphology can be simplified to the standard microstructure of "pits-ridges-protrusions", and thus the geometric equivalent

model of EN-GJL-250 WEDM surface can be established, as shown in Fig. 9. Compared with the original plane, the contact area after processing has two parts, one is the blue concave part in the Fig. 9. and the other is the yellow convex part in the Fig. 9.

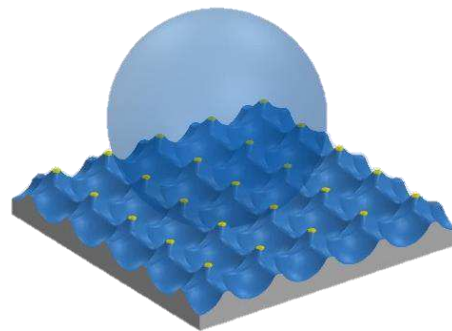
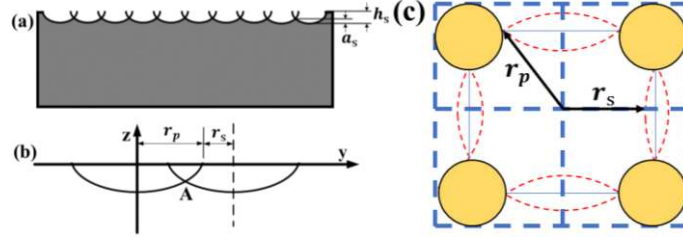


Fig. 9 Geometric equivalent model of the WEDM surface.

The pits are evenly distributed on the machining plane, so the area change law of a pit is consistent with the overall change law. To facilitate the calculation, the wettability of a single pit in the model is studied. Fig. 10(a-b) is a cross-sectional

view of the geometric equivalent model, and Fig.



10(c) is a top view of a single pit in the model.

Fig.10 (a-b) Section diagram of geometric equivalent model for WEDM surface, (c) Top view of single pulse pit.

The relationship between the parameters is given by Eq. 50:

$$a_s = \frac{h_s}{3} = \frac{(d_p + h_p)}{3} \quad (50)$$

Where a_s is the height of the highest point from the bottom of the pit; h_s is the distance between the initial plane and bottom of the pit; d_p is the depth of single-pulse pits; h_p is the height of single pulse pit flanging. To simplify the calculation, assume that the yellow convex part is round. According to Eq. 51 calculate the area S_1 of the yellow convex part.

$$S_1 = \pi \left[\frac{r_p + r_s}{2} - \sqrt{\left(r_p^2 - \frac{(r_p + r_s)^2}{4} \right)} \right]^2 \quad (51)$$

Where r_p is the radius of single pulse pit; r_s is the length of residual radius after superposition of pits.

According to Eq. 52, calculate the area S_2 of the blue ball cover.

$$S_2 = 2\pi R_c a_s \quad (52)$$

Where R_c is the radius of the ball with the same size of the pit.

The R_c can be calculated according to Eq. 53.

$$(R_c - a_s)^2 + \frac{(r_p + r_s)^2}{4} = R_c^2 \quad (53)$$

Combine Eq. 51 and Eq. 52 to calculate the area S_2 of the blue ball cover:

$$S_2 = \pi a_s^2 + \frac{\pi (r_p + r_s)^2}{4}$$

The S surface area of EN-GJL-250 before processing R_c can be calculated according to Eq.

55.

$$S = (r_p + r_s)^2 \quad (54)$$

The roughness coefficient λ of EN-GJL-250 surface is a multiple of the area of the rough surface after processing relative to the original smooth surface, and its value is equal to the ratio of the surface area of the rough surface to the surface area of the smooth surface. Calculate λ according to Eq. 55.

$$\lambda = \frac{S_1 + S_2}{S} \quad (55)$$

Under the condition of Wenzel wetting, λ is always greater than 1, and when the contact angle $\theta_0 < 90^\circ$ in the ideal state, $\theta_w < \theta_0$; When $\theta_0 > 90^\circ$, $\theta_w > \theta_0$. For the geometric equivalent model of EN-GJL-250 WEDM surface, the CA θ_w on the rough surface can be expressed as:

$$\theta_w = \cos^{-1}[\lambda \cos \theta_0]$$

3.2 Establishment of prediction model of surface apparent contact angle of two-scale microstructure

After the surface of the workpiece is micro structured by WEDM, its surface is not absolutely smooth, and there are many discharge pits, as shown in Fig. 11. According to the Wenzel model, these micro-nano structures increase the contact area of the solid-liquid interface and affect the contact angle of water droplets on the material surface.

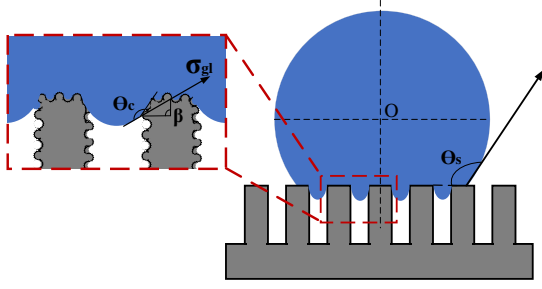


Fig. 11 Diagram of droplet shape on two-scale array microstructure

At the same time, when the workpiece surface is processed into a two-scale microstructure by WEDM, the water droplets do not completely conform to the Cassie-Baxter model, and there is Wenzel wetting state on the micro-nano structure, so the length of the contact line of the water droplets on the microstructure will change, and the increasing ratio of the contact angle is related to λ . There is no solid surface at the gap, so it is considered that the value of the gap is constant. Considering the influence of the surface roughness coefficient, the size parameters of the microstructure become:

$$\begin{aligned} a' &= \lambda a \\ b' &= b \end{aligned}$$

Substituting a' and b' into the Eq. 29, 35, 42 and 49, two-scale contact angle prediction formulas of four microstructures with different shapes are obtained. According to the previous hypothesis, the droplet is in the Cassie-Baxter state on the microstructure surface, and the contact interface between the droplet and the array microstructure is composed of solid and air, but the droplet is in Wenzel wetting state on the micro-nano structure generated by WDEM. Therefore, we consider combining the Cassie-Baxter model with the Wenzel model to analyze the change trend of the CA prediction model with secondary structure.

$$\begin{aligned} \cos \theta_{wc} &= f_1(\cos \theta_w + 1) - 1 \\ f_1 &= \frac{S'_s}{S'_c} \end{aligned}$$

4 Model Analysis and Discussion

4.1 Effect of discharge parameters on surface wettability in WEDM

By WEDM single pulse discharge simulation, I_p and T_{on} can be adjusted to predict the size of discharge pits. Based on the geometric equivalent model of WEDM surface and numerical calculation, the influence of WEDM discharge parameters on the CA of the micro-nano structure under the Wenzel condition is obtained. Through the WEDM linear cutting experiment, Fig. 12 shows the variation of the measured and predicted values of the static contact angle with the discharge parameters.

The results show that with the increase of discharge parameters, the roughness of the workpiece surface increases, the contact area between the water droplet and the rough surface of the workpiece increases, and the CA also increases. But water droplets are always in Wenzel wetting state, WEDM machined surface cannot reach the superhydrophobic state. Therefore, it is difficult to test the superhydrophobic performance of the WEDM surface without machining the microstructure. At the same time, by controlling discharge parameters, WEDM can effectively improve surface hydrophobicity.

4.2 Analysis of the apparent contact angle prediction model of the first-order array microstructure

Without considering the rough micro-nano structure of WEDM, the microstructure of the first-order array is regarded as a smooth structure with hydrophobic properties. Without considering the rough micro-nano structure of WEDM, the microstructure of the first-order array is regarded as a smooth structure with hydrophobic properties. θ_0 is set to 115° , and the volume of the droplet used is $5 \mu\text{l}$. The a , b and other parameters are added into Eq. 29, 35, 42 and

48 to solve θ_s . Fig. 13 shows the curves of the CA θ_s changing with a and b .

When $b=200 \mu\text{m}$ the curves in Fig. 13(A) show the effect of a on θ_s . The results show that: adjusting the shape and size of microstructure can change the CA. At the same time, the increase of the solid part of the microarray structure leads to the decrease of the CA. From the perspective of model establishment, when the area of solid part

increases, the surface wetting state is more similar to the Young model, so θ_s tend to decrease. In other words, the smaller the solid fraction is, the easier it is to obtain a larger CA. When $a=200 \mu\text{m}$ the curves in Fig. 13(B) show the effect of b on θ_s . With the increase of b , θ_s increases first and then decreases. When b is in the range of $200 \mu\text{m}$ - $300 \mu\text{m}$, the θ_s reaches the maximum and the hydrophobic performance is the best.

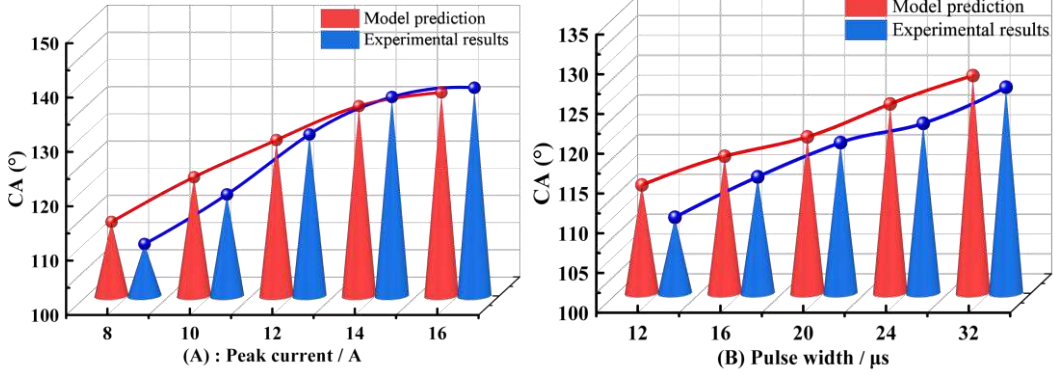


Fig. 12 Under Wenzel wetting state, the variation of contact angle of WEDM surface with peak current and pulse width.

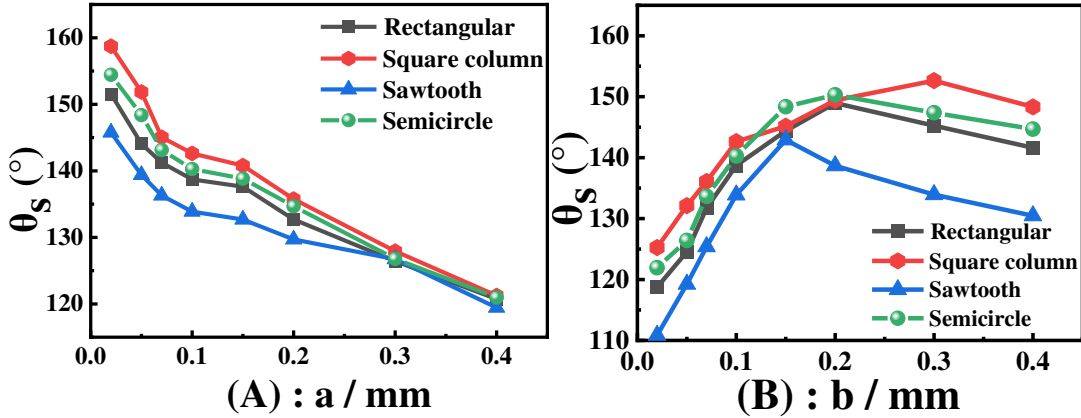


Fig. 13 (A) The variation rule of θ_s of the first-level array microstructure surface with a ; (B) The variation rule of the first-level array microstructure surface θ_s with b .

4.3 Analysis of the apparent contact angle prediction model of the two-order array microstructure

In this paper, it is assumed that the droplets are in the Cassie-Baxter wetting state on the primary array microstructure and Wenzel wetting state on the secondary micro-nano structure. Similarly, the θ_{wc} can be obtained by inputting the size parameters of the microstructure. There

are many factors affecting θ_{wc} . This paper studies the effect of the λ on θ_{wc} .

When $a=200 \mu\text{m}$ and $b=200 \mu\text{m}$ the curves in Fig. 14 show the effect of λ on θ_{wc} . With the increase of λ , the coarser the surface of the material, the contact area of solid and liquid also increases, so θ_{wc} decreases. In addition, the larger the λ , the smaller the effect on θ_{wc} , and the larger the effect of the size parameter on the

contact angle. At the same time, since the solid-liquid contact area of the sawtooth microstructure is much smaller than the other three shapes, the effect of λ on the surface θ_{wc} of the sawtooth microstructure is small.

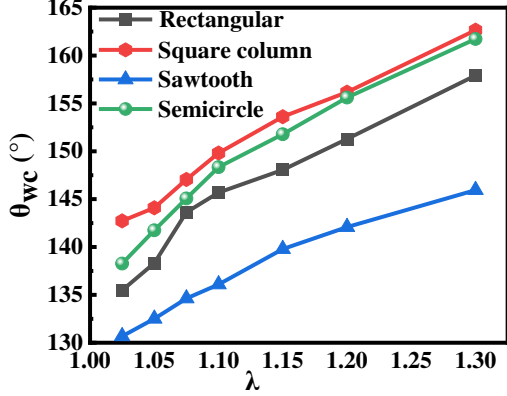


Fig. 14 Variation of θ_{wc} with λ on the WEDM surface of two-scale array microstructures.

5. Experiment and methods

5.1 Material and machine tool

EN-GJL-250 material has the characteristics of high strength, wear resistance and heat resistance. Among all cast iron materials, EN-GJL-250 is often used in the manufacture of some machine tool beds, columns and gears because of its anti-corrosion, shock absorption, and excellent casting properties. The percentage of chemical composition properties of workpiece material is given in Table 1. In this experiment, EN-GJL-250 with a size of $20 \times 20 \times 5$ mm is selected as the workpiece to be processed.

In this experiment, DK7632 high-speed wire electric discharge machine (HS-WEDM) was used to prepare surface microstructures of different shapes, as shown in Fig.15. The electrode wire is the molybdenum wire, the axial flushing method is adopted, and the working fluid is a mixture of water and emulsion. The machine tool adopts an electrode wire tensioning mechanism to reduce the probability of wire breakage during processing. Under the existing programming file, the machine tool can realize the function of self-processing. By changing the parameters on the control panel of the WEDM

machine tool, the required processing conditions can be met.

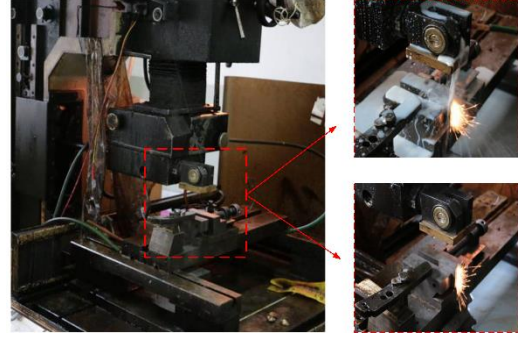


Fig.15 HS-WEDM experimental equipment diagram.

5.2 Experimental design

In this experiment, four array microstructures of rectangle, semicircle, square column and triangle are designed, and their size parameters are consistent with those in the theoretical model, namely $a = 200 \mu\text{m}$, $b = 200 \mu\text{m}$. WEDM has a discharge gap in the process of machining discharge. If the cutting is performed according to the designed size, the actual size obtained will be smaller than the pre-designed size. Therefore, the cutting trajectory of the electrode wire should be planned first. Use WEDM to cut the narrow slit and measure the width of the slit with CCD. The average value is $260 \mu\text{m}$, and the diameter of the electrode wire is $180 \mu\text{m}$, so the discharge gap on one side is about $40 \mu\text{m}$. The experimental machine tool is defined when editing the motion trajectory of the electrode wire. The position of the central axis of the electrode wire, so the distance between the central axis of the electrode wire and the machining surface should be $130 \mu\text{m}$. Design of experimental parameters: the interval ratio is 3:1, the feed rate is 4 m/min, and the machining characteristic is positive polarity. The experimental scheme is shown in Table 2.

The cut metal surface with array microstructure was cleaned in absolute ethanol, deionized water and acetone at room temperature for 10 minutes using an ultrasonic cleaner to clean the oil and debris on the surface of the workpiece.

The surface was quickly blown dry with a hair dryer, soaked in a 2% ethanol solution of stearic acid for 6 hours, then taken out and baked in a constant temperature oven for 30 minutes, and the oven temperature was set to 60°C.

Table 2 Factors and levels for experiment

No.	Microstructure shape	I_p/A	$T_{on}/\mu s$
1	Straight cut	12	24
2	Rectangle	12	24
3	Square columns	12	24
4	Sawtooth	12	24
5	Semicircle	12	24
6	Semicircle	8	24
7	Semicircle	10	24
8	Semicircle	14	24
9	Semicircle	16	24
10	Semicircle	12	12
11	Semicircle	12	16
12	Semicircle	12	20
13	Semicircle	12	32

5.3 Testing methods

5.3.1 Apparent contact angle

The CA of the droplet on the surface of the modified sample was characterized by an OCA20 (DATAPHYSICS, Germany) video optical contact angle measuring instrument, with a

measurement range of 0~180°, an accuracy of $\pm 0.1^\circ$, and a resolution of $\pm 0.01^\circ$. In the wettability test, the droplet volume was 5 μL , and the recording time was 10 s. Three different measurement points were measured on the sample surface. The average value of the left and right contact angles of the same measurement point is taken as the measurement result of one measurement point. The average value of the measurement results of the three measurement points is used as the final data

5.3.2 Surface texture

WEDM is a non-contact machining method. Due to the offset of the wire electrode, the discharge gap and the wire vibration, the actual shape and size of the microstructure will deviate from the designed shape. To further explore the relationship between the actual microstructure shape and CA on the surface of the EN-GJL-250 material, the actual microstructure shape and size were measured using a SperView W1 optical 3D surface profiler.

5.3.3 Micro morphology

The microstructure, morphology and chemical composition of the machined surface of EN-GJL-250 material was characterized by SU3500 Hitachi tungsten filament scanning electron microscope (SEM) equipped with energy dispersive spectrometer (EDS).

Table 1 Chemical composition properties of EN-GJL-25.

Chemical composition (%)	Fe	C	Si	Mn	P	S
	92.50	3.50	2.50	0.75	0.45	0.20

6. Results and discussion

6.1 Contact angle

According to the experimental design of WEDM (Table 2), a set of cutting experiments and contact angle measurement experiments were carried out. Fig.16 depicts the optical properties of surface water droplets after WEDM and low surface energy treatment of EN-GJL-250 material. photo. The experimental data show that the static

contact angle of the WEDM machined surface of EN-GJL-250 material ranges from 122° to 156.15°. Fig.16(14) shows that the intrinsic contact angle measured on the surface of the EN-GJL-250 material is 67.72°, and it can be said that the surface interfacial energy of the EN-GJL-250 material is relatively high. Fig.16(15) is an optical photo of the surface water droplets of EN-GJL-250 material cut by WEDM, but not chemically

treated, indicating that WEDM processing of rough surfaces can achieve hydrophobic properties.

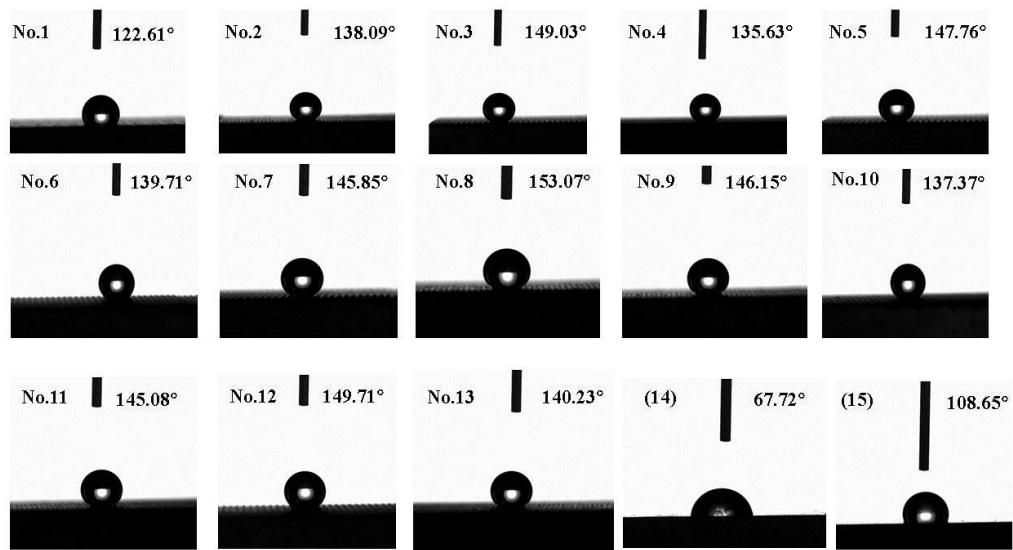


Fig. 16 Optical photo of water droplets on the surface of the experimental sample.

6.2 Surface texture

Fig.17 shows the 3D surface topography and 2D cross-sectional profile of the two-scale micro-structured surfaces with four different shapes prepared by WEDM. Due to the special material removal form of WEDM, the profile line of the processed microstructure cannot be a perfect curve. The blue curve in the 2D cross-sectional profile is the original surface morphology, and the red curve is obtained by filtering the profile curve with a three-dimensional spline filter. The cut-off wavelength is 80 μm , and the measurement of microstructure-scale parameters adopts the red cross section line. In the actual measurement process, the difference between the design dimensions a and b and the actual dimensions ranged from 85.7 μm to 102.3 μm , and the average value of these differences was 91.4 μm . The reason for this error is that there are factors such as electrode wire offset, discharge concentration and electrode wire vibration during the machining process of WEDM. The fluctuation of the error value is caused by the phenomenon of angular discharge and measurement error.

6.3. Micro morphology

Fig.18 shows SEM images showing the top regions of the array microstructures of four different shapes, with magnifications of 500x, 1000x and 4000x for (a), (b) and (c), respectively. It can be seen from Fig. 17 that the WEDM machined surface of EN-GJL-250 material is mainly composed of randomly distributed pits, ellipsoid convex bodies and wrinkles. The molten crater is caused by the fact that the pulse voltage breaks down the working fluid and generates spark discharge in the process of WEDM, and a large amount of heat energy is instantaneously concentrated in the discharge microchannel, which melts a small amount of metal material on the working surface. The convex body is formed by the bubbles in the discharge channel exploding and flying out, and then fused and adhered to the processed surface and then condensed. The wrinkle is due to the overlapping of the discharge pits during the processing, resulting in the formation of wrinkled strip-shaped protrusions on the edges of the discharge craters. These randomly distributed discharge pits, protrusions and wrinkles can be well combined with stearic acid during low surface energy treatment, thereby reducing the surface free energy of the material.

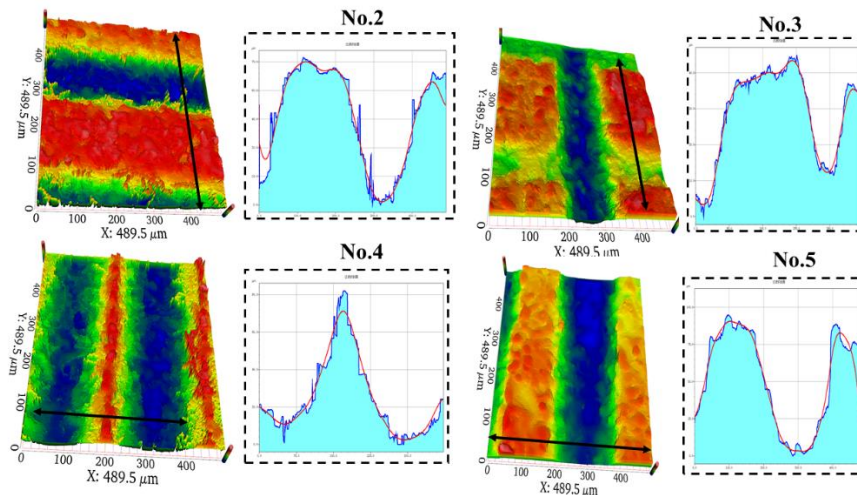


Fig. 17 Three-dimensional surface profile of the experimental sample (NO.2-5).

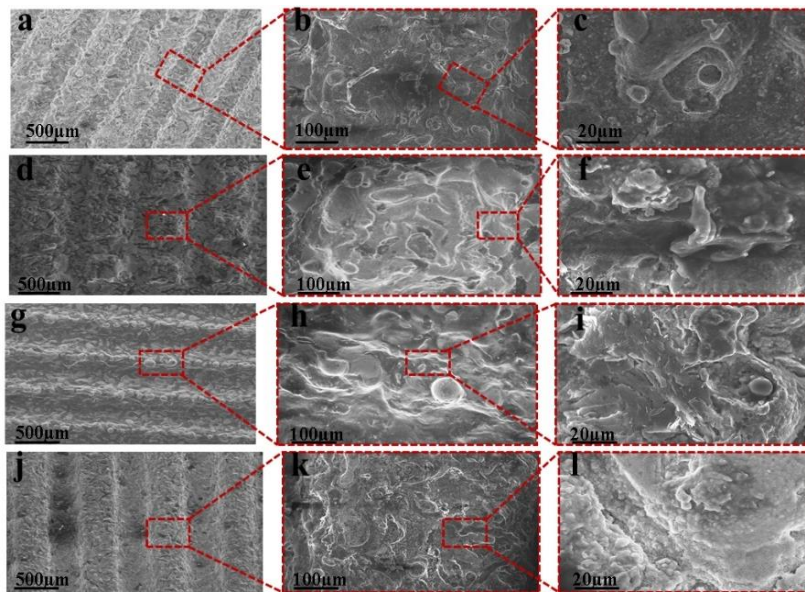


Fig. 18 SEM images of the microstructures (a-c) rectangle; (d-f) square column; and (g-i) sawtooth; and (j-l) semicircular.

6.4 Model Validation

6.4.1 Influence of microstructure shape on apparent contact angle

Fig.19 shows the comparison of contact angles of microstructures with different shapes under the same discharge parameters. The results show that: square column > semicircle > rectangular > sawtooth > linear cutting. Cause analysis: Fig.18 (a, d, g, j) shows that when the water droplets are in the Cassie-Baxter wetting state on the surface of the workpiece, the solid-liquid contact area of the square column array microstructure is the smallest, and the solid-liquid

contact area of the rectangular array microstructure is the largest. By analyzing the contact angle prediction model, it can be seen that the larger the solid-liquid contact area is, the smaller the contact angle of water droplets is. However, because the solid-liquid contact of the sawtooth array microstructure is too small to maintain the spherical morphology of water droplets, the hydrophobic performance is the worst. Fig.14 (NO.4) shows that water droplets are in Wenzel wetting state on serrated microstructures. At the same time, when the geometric size of the semicircular array

microstructure is suitable, by controlling the discharge parameters, multilevel micro-nano structures can be prepared on the surface of EN-GJL-250 material to obtain the superhydrophobic surface.

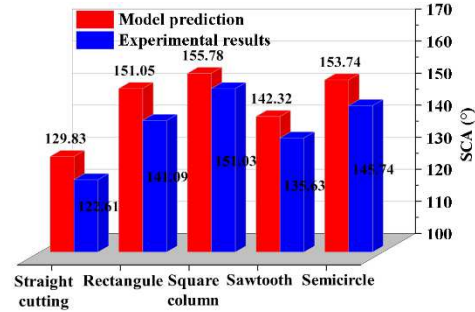


Fig.19 The comparison chart of the model prediction value and the experimental measurement value of the surface CA of different shape microstructure machined by WEDM.

6.4.2 Effect of pulse width on apparent contact angle

When $a = 200 \mu\text{m}$, $b = 200 \mu\text{m}$. and $I_p = 12 \text{ A}$. the curves in Fig. 20 show the effect of T_{on} on CA. From the curve changes in Fig.20, when the pulse width is equal to $20 \mu\text{s}$, the CA of the semicircular array microstructure is the largest. When the pulse width increases, the contact angle first increases and then decreases. As the single pulse discharge energy increases, the roughness of the microstructure surface increases slightly, resulting in the formation of secondary microstructure. At this time, the secondary microstructure forms the Cassie-Baxter model again, and the CA of the EN-GJL-250 material surface increases.

In addition, it is also possible that due to the increase of the discharge energy, the microstructure gap increases, resulting in a slight increase in the CA. However, when the pulse width continues to increase, the discharge pits will become larger and deeper, and the secondary microstructure is closer to the Wenzel model. The liquid penetrates into the gaps between the secondary microstructure, resulting in the

decrease of the CA of the EN-GJL-250 material surface.

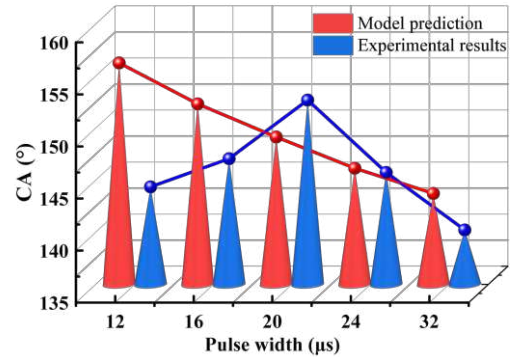


Fig. 20 The variation law of the model predicted value and experiment measured value of the CA of semicircular array microstructures vary with T_{on} .

6.4.2 Effect of pulse width on apparent contact angle

When $a = 200 \mu\text{m}$, $b = 200 \mu\text{m}$. and $T_{on} = 12 \mu\text{s}$ the curves in Fig. 21 show the effect of I_p on CA. With the increase of the peak current, the energy of a single pulse is increasing, and the reason for the influence of pulse width on the CA is the same. Fig.22 shows the three-dimensional morphology of $I_p = 10 \text{ A}$ and $I_p = 16 \text{ A}$, with Ra of $3.67 \mu\text{m}$ and $6.49 \mu\text{m}$, respectively. It can be seen that with the increase of single pulse energy, the size, depth and number of pits on the surface of EN-GJL-250 material increase, resulting in changes in the state of droplets on the secondary microstructure, thus affecting the CA of droplets on the metal surface.

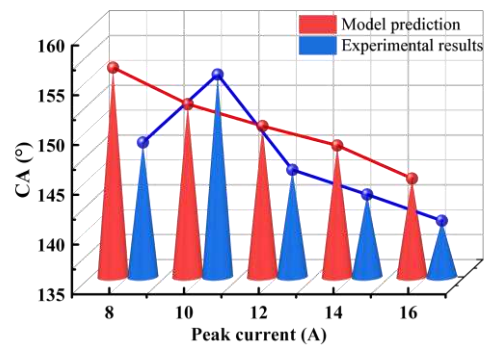


Fig. 21 The variation law of the model predicted value and experiment measured value of the CA of semicircular array microstructures vary with I_p .

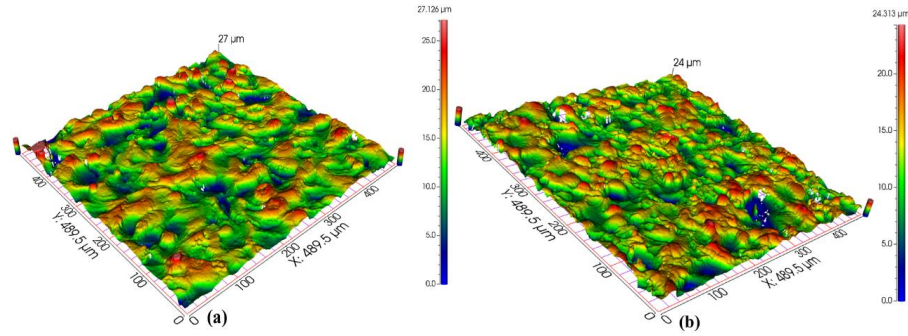


Fig. 22 3D micrometer surface morphology with different discharge energies: (a) $I_p=10$ A; (b) $I_p=16$ A.

Conclusion

The following conclusions were derived from this study.

(1) In this paper, based on the simulation method, the heat flow coupling model in the WEDM single pulse discharge process is established. The formation process and morphology evolution process of single pulse discharge pits were numerically simulated. The simulation results show that the molten material will first form a smooth depression in the center and then be pushed to the sides and be removed continuously during the formation of discharge pits. Meanwhile, flanging bulges appear around the edges of the pits. By establishing the geometric equivalent model of the surface machined by WEDM, it is found that it is difficult to achieve superhydrophobic properties of the surface machined by WEDM without any shape microstructure.

(2) In this paper, four kinds of array microstructures suitable for WEDM machining are designed. Based on the force balance method, the CA prediction models of semicircle, rectangular, sawtooth and square column array microstructures are established respectively. The analysis model found that the smaller the solid-liquid contact area, the easier to obtain a larger CA; when a is less than $200\ \mu\text{m}$, b is in the range of $200\ \mu\text{m} - 300\ \mu\text{m}$, the contact angle reaches the maximum. The surface roughness coefficient is introduced into the contact angle prediction formula by taking the micro-nano structure of the WEDM machined surface as the secondary

structure. The results show that with the increase of surface roughness coefficient, the surface hydrophobicity of the two-scale array microstructure is worse.

(3) The superhydrophobic surface was prepared on EN-GJL-250 material by WEDM. The prediction model of the CA of the two-scale array microstructure was verified by experiments. The predicted CA values of the established mathematical model are in good agreement with the experimental values, and the overall trend is the same, with an average error of 7.83 %. Among the four kinds of array microstructure, cutting square cylindrical array microstructure is the most easy to achieve superhydrophobic surface; when the pulse width is $20\ \mu\text{s}$ and the peak current is 10 A, the CA of the semicircular array microstructure is the largest.

LIST OF ABBREVIATIONS

WEDM = Wire-cut electrical discharge machine

EN-GJL-250 = Gray cast iron material

I_p = Peak current

T_{on} = Pulse width

FEM = Finite element method

Ra = Surface roughness

CONSENT FOR PUBLICATION

Not applicable.

CONFLICT OF INTEREST

The authors declare no conflict of interest, financial or otherwise.

FUNDING

This research was supported by the National

Natural Science Foundation of China: 52075134;
Natural Science Foundation of Heilongjiang
Province of China: LH2019E062;
Postdoctoral Scientific Research Developmental
Fund of Heilongjiang Province of China: LBH-
Q20097;
Fundamental Research Foundation for
Universities of Heilongjiang Province, China:
LGYC2018JC040

ACKNOWLEDGEMENTS

Declared none.

REFERENCES

- [1] Wang N, Tang L, Tong W, Xiong D (2018) Fabrication of robust and scalable superhydrophobic surfaces and investigation of their anti-icing properties. *Materials & Design* 156: 320-328.
- [2] Jin H, Li Z, Wei S, Nie S, Pan Z, Zhang T, Gao N (2018) Corrosion resistance and dynamic anti-icing of superhydrophobic surface on ASW. *Surface Engineering* 34(8): 603-610.
- [3] Young T (1805) An essay on the cohesion of fluids. *Philosophical transactions of the royal society of London* (95): 65-87.
- [4] Wenzel RN (1936) Resistance of solid surfaces to wetting by water. *Industrial & Engineering Chemistry* 28(8): 988-994.
- [5] Cassie ABD, Baxter S (1944) Wettability of porous surfaces. *Transactions of the Faraday society* 40: 546-551.
- [6] Neinhuis C, Barthlott W (1997) Characterization and distribution of water-repellent, self-cleaning plant surfaces. *Annals of botany* 79(6): 667-677.
- [7] Barthlott W, Neinhuis C (1997) Purity of the sacred lotus, or escape from contamination in biological surfaces. *Planta* 202(1): 1-8.
- [8] Zhu K, Zhang J, Zhang H, Tan H, Zhang W, Liu Y, Zhang H, Zhang Q (2018) Fabrication of durable superhydrophobic coatings based on a novel branched fluorinated epoxy. *CHEM ENG J* 351: 569-578.
- [9] Zhang P, Maeda Y, Lv F, Takata Y, Orejon D (2017) Enhanced Coalescence-Induced Droplet-Jumping on Nanostructured Superhydrophobic Surfaces in the Absence of Microstructures. *ACS APPL MATER INTER* 9: 35391-35403.
- [10] Özcan S, Açıkbay G, Açıkbay NC (2018) Induced superhydrophobic and antimicrobial character of zinc metal modified ceramic wall tile surfaces. *APPL SURF SCI* 438: 136-146.
- [11] Ranjith KS, Nivedita LR, Asokan K, Krishnamurthy S, Pandian R, Kamruddin M, Avasthi DK, Kumar RTR (2017) Robust water repellent ZnO nanorod array by Swift Heavy Ion Irradiation: Effect of Electronic Excitation Induced Local Chemical State Modification. *SCI REP-UK* 7.
- [12] Kostal E, Stroj S, Kasemann S, Matylitsky V, Domke M (2018) Fabrication of Biomimetic Fog-Collecting Superhydrophilic-Superhydrophobic Surface Micropatterns Using Femtosecond Lasers. *LANGMUIR* 34: 2933-2941.
- [13] Wang Y, Wang W, Zhong L, Wang J, Jiang Q, Guo X (2010) Super-hydrophobic surface on pure magnesium substrate by wet chemical method. *Applied Surface Science* 256(12): 3837-3840.
- [14] Rajab FH, Liu Z, Wang T, Li L (2019) Controlling bacteria retention on polymer via replication of laser micro/nano textured metal mould. *Optics & Laser Technology* 111: 530-536.
- [15] Lin J, Lin F, Liu R, Li P, Fang S, Ye W, Zhao S (2020) Scalable fabrication of robust superhydrophobic membranes by one-step spray-coating for gravitational water-in-oil emulsion separation. *Separation and Purification Technology* 231: 115898.
- [16] Lu Z, Wang P, Zhang D (2015) Super-hydrophobic film fabricated on aluminium surface as a barrier to atmospheric corrosion in a marine environment. *Corrosion Science* 91: 287-296.
- [17] Jalil SA, Akram M, Bhat JA, Hayes JJ, Singh SC, ElKabbash M, Guo C (2020) Creating superhydrophobic and antibacterial surfaces on gold by femtosecond laser pulses. *Applied surface science* 506: 144952.
- [18] Yu Z, Zhou C, Liu R, Zhang Q, Gong J, Tao D, Ji Z (2020) Fabrication of superhydrophobic surface with enhanced corrosion resistance on H62 brass substrate. *Colloids and Surfaces A: Physicochemical and*

Engineering Aspects 589: 124475.

- [19] Moaven K, Rad M, Taeb-Rahni M (2013) Experimental investigation of viscous drag reduction of superhydrophobic nano-coating in laminar and turbulent flows. *Experimental Thermal and Fluid Science* 51: 239-243.
- [20] Chen Z, Yan Z, Zhou H, Han F, Zhao L, & Yan H (2021) One-step fabrication of the wear-resistant superhydrophobic structure on SiCp/Al composite surface by WEDM. *Surface and Coatings Technology* 409: 126876.
- [21] Hou Y, Xu J, Lian Z, Yang S, Zhai C, Cai Q, Yu H (2021) Fabrication of superhydrophobic NiTi shape memory alloy surface with inclined microstructure by wire electrical discharge machining. In 2021 IEEE International Conference on Manipulation, Manufacturing and Measurement on the Nanoscale (3M-NANO). IEEE: 324-327
- [22] Roy T, Sabharwal TP, Kumar M, Ranjan P, Balasubramaniam R (2020) Mathematical modelling of superhydrophobic surfaces for determining the correlation between water contact angle and geometrical parameters. *Precision Engineering* 61: 55-64.
- [23] Wang H, Chi G, Wang Y, Yu F, Wang ZL (2019) Fabrication of superhydrophobic metallic surface on the electrical discharge machining basement. *Applied Surface Science* 478: 110-118
- [24] Xiong JW, Zhu J Y, Hu XF (2017) Preparation of Superhydrophobic Cooper Surface with Anticorrosive Property. *Paint Coatings Industry* 47(09): 12-17.
- [25] Li J, Zhao SC, Li Q, Li H, Zhang W, Yu HD (2017) Fabrication of biomimetic multi-scale surface of rice leaf and anisotropic superhydrophobic properties (in Chinese). *China Sci Bull* 62: 1766-1773
- [26] Chen Z, Yan Z, Zhou H, Han F, Zhao L, Yan H (2021) One-step fabrication of the wear-resistant superhydrophobic structure on SiCp/Al composite surface by WEDM. *Surface and Coatings Technology* 409: 126876.
- [27] Xiao CL, Liang SY, Yu ZQ (2020) Experimental Study on Superhydrophobic Surface of Controllable Array Microcolumns. *Plating and Finishing* 42(07): 27-32.
- [28] Xiong JW, Zhu JY, Hu XF (2017) Preparation of Superhydrophobic Cooper Surface with Anticorrosive Property. *PAINT COATINGS INDUSTRY* 47(09): 12-17.
- [29] Wu C, Wu X, Zhao H, Xu B, Zhu L, Liu Y, Gao C (2020) Effect of sub-millimetre morphologies on the hydrophobicity of a copper surface prepared by WEDM. *Surface and Coatings Technology* 385: 125455.
- [30] Dong SL (2018) Research on micro-edm and its superhydrophobic property of beryllium copper alloy. Harbin Institute of Technology.
- [31] Extrand CW, Moon SI (2012) Intrusion pressure to initiate flow through pores between spheres. *Langmuir* 28(7): 3503-3509.
- [32] Liu SS, Zhang CH, He JG (2013) Wetting state transition on hydrophilic microscale rough surface. *Acta Physica Sinica* 62(20): 206201-206201.
- [33] Söz CK, Yilgör E, Yilgör I (2015) Influence of the average surface roughness on the formation of superhydrophobic polymer surfaces through spin-coating with hydrophobic fumed silica. *Polymer* 62: 118-128.
- [34] Song H, Liu ZQ, Shi ZY (2016) Micro-end milling and hydrophobic properties of machined surface for microgroove and microarray. *Chinese Journal of Mechanical Engineering* 52(21): 198-205.
- [35] Bai XL (2018) Study on Theoretical Modeling and Evaluation of Surface Wettability of EDM-Bismuth Copper Material. Harbin Institute of Technology.
- [36] Wang H, Chi G, Li L, Gong S, Zhu J, Tian C, Wang Z (2021) Numerical Calculation of Apparent Contact Angles on the Hierarchical Surface with Array Microstructures by Wire Electrical Discharge Machining. *Langmuir* 37(5): 1768-1778.
- [37] Dong J, Jin Y, Dong H, Liu J, Ye S (2018) Numerical study for a large-volume droplet on the dual-rough surface: apparent contact angle, contact angle hysteresis, and transition barrier. *Langmuir* 34(27): 8119-8127.